On the impact of the vertical structure of Martian water ice clouds on nadir atmospheric retrievals from simultaneous EMM/EXI and TGO/ACS-MIR observations

Aurélien Stcherbinine, Michael Wolff, Christopher Edwards, Oleg Korablev, Anna Fedorova, Alexander Trokhimovskiy

▶ **To cite this version:**

Aurélien Stcherbinine, Michael Wolff, Christopher Edwards, Oleg Korablev, Anna Fedorova, et al.. On the impact of the vertical structure of Martian water ice clouds on nadir atmospheric retrievals from simultaneous EMM/EXI and TGO/ACS-MIR observations. Icarus, 2025, 425, pp.116335. 10.1016/j.icarus.2024.116335 . hal-04558105v2

HAL Id: hal-04558105
https://hal.science/hal-04558105v2

Submitted on 5 Oct 2024

HAL is a multi-disciplinary open access archive for the deposit and dissemination of scientific research documents, whether they are published or not. The documents may come from teaching and research institutions in France or abroad, or from public or private research centers.

L'archive ouverte pluridisciplinaire **HAL**, est destinée au dépôt et à la diffusion de documents scientifiques de niveau recherche, publiés ou non, émanant des établissements d'enseignement et de recherche français ou étrangers, des laboratoires publics ou privés.

Distributed under a Creative Commons Attribution - NonCommercial 4.0 International License

Icarus 425 (2025) 116335

Contents lists available at ScienceDirect

Icarus

journal homepage: www.elsevier.com/locate/icarus

On the impact of the vertical structure of Martian water ice clouds on nadir atmospheric retrievals from simultaneous EMM/EXI and TGO/ACS-MIR observations.

Aurélien Stcherbinine [a,b,*], Michael J. Wolff [c], Christopher S. Edwards [a], Oleg Korablev [d], Anna Fedorova [d], Alexander Trokhimovskiy [d]

[a] Department of Astronomy and Planetary Science, Northern Arizona University, Flagstaff, AZ, USA
[b] Institut de Recherche en Astrophysique et Planétologie, CNES, Université Toulouse III Paul Sabatier, CNRS, Toulouse, France
[c] Space Science Institute, Boulder, CO, USA
[d] Space Research Institute (IKI), Moscow, Russia

ARTICLE INFO

Dataset link: http://sdc.emiratesmarsmission.ae, http://sdc.emiratesmarsmission.ae/data, https://sdc.emiratesmarsmission.ae/documentation, https://sdc.emiratesmarsmission.ae/data/exi, https://archives.esac.esa.int/psa/#!Table%20View/ACS=instrument

Keywords:
Mars
Atmosphere
Clouds
Observations
Radiative transfer

ABSTRACT

Retrieving the optical depth of the Martian clouds (τ_{cld}) is a powerful way to monitor their spatial and temporal evolution. However, such retrievals from nadir imagery rely on several assumptions, including the vertical structure of the clouds in the atmosphere. Here we compare the results of cloud optical depth retrievals at 320 nm from the Emirates eXploration Imager (EXI) onboard the Emirates Mars Mission (EMM) "Hope" orbiter performed using a basic uniform cloud profile used in previous studies and using derived cloud profiles obtained from near-simultaneous Solar Occultation observations in the 3.1–3.4 μm spectral range from the Middle-Infrared channel of the Atmospheric Chemistry Suite (ACS) instrument onboard the ESA Trace Gas Orbiter (TGO). We show that the latitudinal dependence of the cloud vertical profiles can have a strong impact on the nadir retrievals; neglecting it can lead to a significant underestimation of τ_{cld} in the polar regions (up to 25 % to 50 %, depending on the vertical distribution of the dust in the atmosphere) and to a lesser extent, to an overestimation of τ_{cld} around the equator. We also discuss the impact of a vertically-dependent particle size profile, as previous studies have shown the presence of very small water ice particles at the top of the clouds. From this analysis, we provide recommendations for the improvement of water ice cloud parameterization in radiative transfer algorithms in nadir atmospheric retrievals.

1. Introduction

Water ice clouds play an important role in the current Martian climate: they affect the thermal structure of the atmosphere by absorbing and scattering the incoming Solar radiation (Haberle et al., 2011; Madeleine et al., 2012; Navarro et al., 2014; Wilson et al., 2007, 2008), and are a major actor in the inter-hemispheric water exchange with a different dynamic compared to that of water vapor (Clancy et al., 1996; Montmessin et al., 2004, 2017b). Constraining the properties and behavior of the water ice clouds on Mars is thus of importance to a better understanding of the current climate of the planet and its evolution.

Over the past 25 years, several orbital missions and their instruments have been looking at the Martian clouds through different geometries: nadir in UV–Visible (Mars Color Imager (MARCI), Emirates eXploration Imager (EXI); e.g., Wolff et al., 2019, 2022), thermal (Thermal Emission Spectrometer (TES), Thermal Emission Imaging System (THEMIS), Mars Climate Sounder (MCS), Emirates Mars Infrared Spectrometer (EMIRS); e.g., Smith et al., 2001, 2003, 2022; Heavens et al., 2011; Atwood et al., 2022) or infrared wavelength (Observatoire pour la Minéralogie, l'Eau, les Glaces et l'Activité (OMEGA), Compact Reconnaissance Imaging Spectrometer for Mars (CRISM), Spectroscopy for Investigation of Characteristics of the Atmosphere of Mars (SPICAM); e.g., Vincendon et al., 2011b; Szantai et al., 2021; Mateshvili et al., 2007; Willame et al., 2017), limb (OMEGA, CRISM, SPICAM, Imaging Ultraviolet Spectrograph (IUVS); e.g., Vincendon et al., 2011a; Clancy et al., 2019; Rannou et al., 2006; Stevens et al., 2017), or Solar Occultation (SPICAM, Atmospheric Chemistry Suite (ACS), Nadir and Occultation for MArs Discovery (NOMAD); e.g., Montmessin et al., 2017a; Määttänen et al., 2013; Stcherbinine et al., 2020, 2022; Luginin et al., 2020; Liuzzi et al., 2020; Stolzenbach et al., 2023). As several

* Corresponding author at: Institut de Recherche en Astrophysique et Planétologie, CNES, Université Toulouse III Paul Sabatier, CNRS, Toulouse, France.
E-mail address: Aurelien.Stcherbinine@irap.omp.eu (A. Stcherbinine).
URL: https://aurelien.stcherbinine.net (A. Stcherbinine).

https://doi.org/10.1016/j.icarus.2024.116335
Received 18 April 2024; Received in revised form 22 September 2024; Accepted 23 September 2024
Available online 30 September 2024
0019-1035/© 2024 The Authors. Published by Elsevier Inc. This is an open access article under the CC BY-NC license (http://creativecommons.org/licenses/by-nc/4.0/).

missions remain active at present, one can now make direct comparisons of their respective datasets, with information from their different viewing geometries complementing each other. This results in a more comprehensive view of Martian clouds.

Nadir observations with UV-visible multi-band cameras such as MARCI onboard the Mars Reconnaissance Orbiter (MRO) (Malin et al., 2001; Bell et al., 2009) or EXI of the Hope probe (Jones et al., 2021; Amiri et al., 2022) provide a large spatial coverage per image but only limited access to the vertical structure of the aerosol profile in the atmosphere. Similarly, ground-based observations from Earth also provide a global view of the spatial distribution of Martian clouds, but with a lower resolution and again very limiter access the vertical structure of the atmosphere (Lilensten et al., 2022). This is in contrast to Solar Occultation (hereafter "SO") or limb-viewing geometry for instance, that provide detailed vertical profiles but only with a limited spatial extent (especially in the case of SO). Thus, nadir imagery is the easier way to constrain the spatial distribution and variations of the Martian clouds. However, retrieving the column-integrated optical depth of the clouds (τ_{cld}) from nadir reflectance measurements requires assumptions on the vertical structure and properties of the atmosphere, including the vertical distribution of dust and ice aerosols. Such assumptions on the aerosol properties can be a significant source of retrieval uncertainties (e.g., Wolff et al., 2019).

Typically, the retrieval algorithms for MARCI and EXI assume clouds characterized by water ice particles of the same size uniformly distributed from a given bottom altitude (usually taken between 15 and 20 km) to 100 km, the bottom altitude being the same regardless of the time of the year or the geographic coordinates of the clouds (e.g., Wolff et al., 2019, 2022). An alternative approach that has been implemented for THEMIS and TES cloud retrievals implemented a variable lower altitude of the clouds, using the water condensation altitude as the bottom boundary for the presence of water ice (e.g., Clancy et al., 1996; Smith et al., 2003; Wolff and Clancy, 2003). However, recent studies have shown that the cloud altitude varies significantly with the season and latitude (e.g., Stcherbinine et al., 2022; Smith et al., 2013; Montmessin et al., 2006; Heavens et al., 2011; Lolachi et al., 2022), and that the distribution of the ice particle sizes with the altitude is characterized typically by a decrease in size when the altitude increases (e.g., Clancy et al., 2019; Stcherbinine et al., 2020, 2022; Luginin et al., 2020; Liuzzi et al., 2020; Stolzenbach et al., 2023). Indeed, if water ice clouds are observed mostly from 10 to 40 km in the polar regions around $L_s \sim 180°$, they are detected between 40 and 80 km at the same time around the equator, and between 20 and 50 km in the equatorial regions around $L_s \sim 90°$ (Stcherbinine et al., 2022). This observed latitudinal and temporal diversity in the altitude of the water ice particles is in contrast with the classical approach of using always the same single vertical profile for all the clouds. Thus, the question that arises is: how do more realistic vertical profiles of water ice cloud properties (i.e., obtained with SO geometry) affect the optical depth retrievals from nadir data compared to those using more simple vertical prescriptions?

In this article, we combine simultaneous ACS-MIR vertical profiles of Martian water ice clouds and nadir images acquired by EXI to study the impact of refining the vertical structure of the clouds on the EXI optical depth retrievals. First, we present in Section 2 the datasets and methods used in this study. Then, Section 3 discusses the results on the impact of altitude variations and particle size gradient in the EXI retrievals. Finally, Section 4 summarizes the main points of the study.

2. Data and methods

2.1. Vertical clouds profiles from ACS-MIR

The Atmospheric Chemistry Suite (ACS) instrument is a set of three spectrometers onboard the ExoMars Trace Gas Orbiter (TGO) ESA-Roscosmos spacecraft, which has been conducting science operations

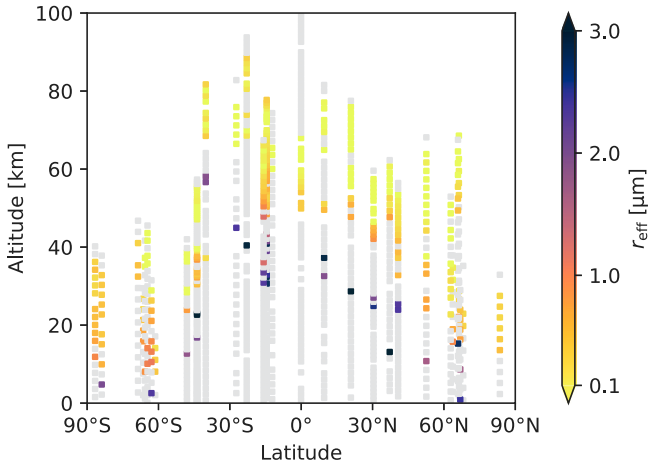

Fig. 1. The vertical profiles of water ice clouds effective radius (r_{eff}) as a function of altitude derived from ACS-MIR measurements used in this study, as a function of the latitude of the observation (see Fig. 2 for the spatial distribution of the observations). L_s are ranging from 76.4° to 358.8° over MY 36 (see details of the observations in Table 1). Data from the first half of MY 36 have already been published in Stcherbinine (2022). Observations without water ice detections are in gray.

for 3 Martian Years (MY), since March 2018 (Korablev et al., 2018, 2019; Vandaele et al., 2019). The Mid-InfraRed (MIR) channel is a high-resolution cross-dispersion echelle spectrometer dedicated to SO geometry (Trokhimovskiy et al., 2015; Korablev et al., 2018).

We use the methodology and results presented in Stcherbinine et al. (2020, 2022) and summarized in the following, to retrieve the water ice opacity, as well as the ice particle effective size, as a function of altitude in the Martian atmosphere. The observations use the 3-µm region observed with the ACS-MIR position 12 of the primary grating mirror (covering wavelengths from 3.1 to 3.4 µm) and have a vertical resolution of ~2.5 km. The atmospheric transmittance values measured by the instrument at each observed altitude (tangent point) are converted into extinction coefficients (k_{ext}) through an onion-peeling (vertical) inversion algorithm (Goldman and Saunders, 1979). The resulting extinction spectra are fitted with models using spherical water ice and dust particles of various sizes in order to constrain the presence and the size of water ice particles in the atmosphere. Some ACS clouds profiles, from the first half of MY 36, have already been published in Stcherbinine (2022), but more recent observations have been processed specifically for this study. The ACS-MIR clouds profiles used in this study are presented as a function of the latitude in Figs. 1, and 2 shows the spatial and temporal distribution of these observations.

An unfortunate limitation of the method, due to the small wavelength range covered by the position 12 acquisitions (3.1–3.4 µm), is that it is not sensitive to the larger water ice particles ($r_{eff} \gtrsim 3$ µm) that may be present at the bottom of the profiles; that is to say that one will not be able to distinguish them from dust particles (see discussion in Stcherbinine et al. (2020, 2022)). However, these potential layers at low altitudes will likely be mixed with a larger amount of dust (e.g., Smith et al., 2013), which will limit their contribution to the clouds' optical depth as observed from the orbit (see discussion in Section 3).

2.2. Optical depths retrievals with EXI

The Emirates eXploration Imager (EXI) instrument onboard the Emirates Mars Mission (EMM) "Hope" probe is a UV–Visible framing camera that has been observing the full Martian disk in 6 bandpasses since the beginning of its science phase in May 2021 (Amiri et al., 2022; Jones et al., 2021). Here, we follow the method of Wolff et al. (2022) that uses the normalized reflectance (I/F) at $\lambda = 320$ nm (the EXI f320 band) to retrieve the water ice clouds optical depth τ_{cld}. The

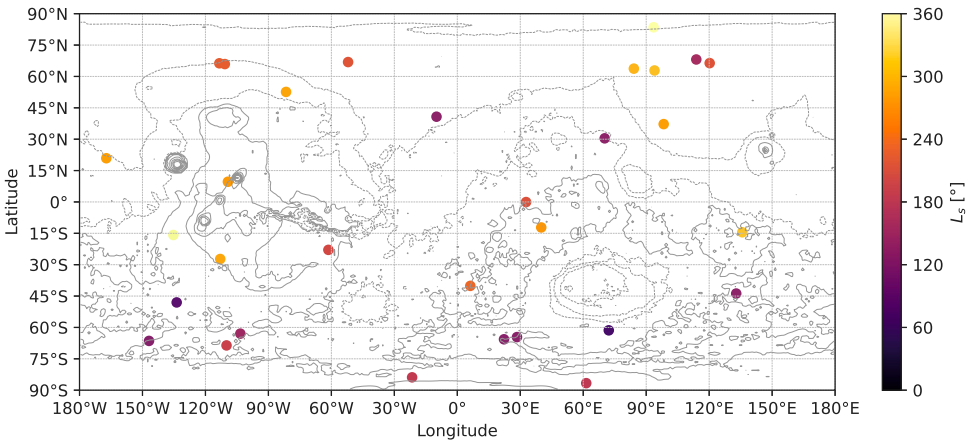

Fig. 2. Spatial (longitude and latitude) and temporal (L_s, spanning over MY 36) distribution of the 31 ACS-MIR observations used in this study. See Table 1 for more details.

EXI data used in this study have been acquired in the so-called XOS-1 mode with a 2 × 2 binning, giving a spatial resolution of 4–8 km per pixel at nadir, and processed to level 2A. Information about the EXI data products is provided in the Data Availability section.

We use the DIScrete Ordinate Radiative Transfer (DISORT) code (Stamnes et al., 1988, 2017) through the *pyRT_DISORT* Python module (Connour and Wolff, 2023) to perform the retrievals at 320 nm. In terms of the model parameters, we employ the following, based on Wolff et al. (2019, 2022):

- Surface: Hapke reflectance model, with the values of the parameters of the MARCI band 7 model from Wolff et al. (2019), scaled to be adjusted to the EXI radiometric calibration (Wolff et al., 2022).
- Atmospheric dust: a vertical profile with a constant volume mixing ratio (with respect to the CO_2 gas density) of 1.5 μm dust particles from the surface to 100 km as it is usually the case in such studies (e.g., Wolff et al., 2017, 2019, 2022) (or alternative upper altitude derived from ACS-MIR observations). Dust properties are computed assuming asymmetric hexahedral shapes with a sphericity of 0.78 and an effective variance v_{eff} of 0.3 (Saito et al., 2021), and refractive indices from Wolff et al. (2010) and Connour et al. (2022). The total column optical depth τ_{dust} is extracted from a contemporaneous dust climatology constructed from the EMIRS observations (Smith et al., 2022; Edwards et al., 2021).
- Pseudo-spherical atmosphere geometry: as ACS-MIR profiles are acquired close to the terminator (see Section 2.3), they are associated with high incidence and potentially with large emergence angles as well. We use the pseudo-spherical correction introduced in DISORT 3 (Stamnes et al., 2017) instead of the classical plane-parallel representation, allowing for an explicit treatment of planetary/atmospheric curvature.
- Water ice clouds: extinction and scattering properties of water ice particles are computed assuming droxtals shapes, a gamma size distribution (Hansen and Travis, 1974) with an effective variance of 0.1 (e.g., Wolff et al., 2019, and reference contained within).

Typically, these kinds of retrievals assume a vertical profile of the water ice aerosols defined by a cloud bottom around 20 km and a constant volume mixing ratio above this altitude (e.g., Wolff et al., 2019, 2022). In the present study, we will compare the optical depth values retrieved using this cloud vertical profile on some examples, with results using alternative vertical structures (altitude, ice particle sizes) from ACS-MIR coincident observations.

2.3. Cross-observations

While EXI offers column-integrated cloud optical depths over the illuminated Martian disk, ACS-MIR will provide locally detailed information about the vertical distribution of the water ice particle properties (cf Fig. 1). Due to the SO observing geometry, ACS-MIR can only acquire atmospheric profiles near the morning and evening terminators (local times ~ 06:00 and 18:00).

To perform optical depth retrievals in nadir geometry, the vertical distribution of the aerosols in the atmosphere is one of the main assumptions that must be made. Usually, one uses a uniform distribution of one size distribution with the base of the cloud starting always at the same given altitude regardless of the latitude or season (typically taken between 15 and 20 km) (e.g., Wolff et al., 2017, 2019, 2022).

Even though no coordinated observations between the EXI and ACS instruments (or the EMM and TGO probes) have been explicitly planned, they are both looking at the Martian atmosphere from their respective orbits. Thus, we searched for observations from both instruments that observed the same coordinates within one hour between February 2021 and January 2023, which includes the whole MY 36. We identify 31 observations from each instrument that match these criteria, spanning from L_s = 76° to L_s = 359° (MY 36) and covering all latitudes from 86°S to 86°N. Table 1 gives the list and coordinates of the observations used in this study and Fig. 2 shows the spatial distribution of the ACS-MIR observations on a map of Mars.

3. Results and discussion

The retrievals of water ice cloud optical depth are performed on the 31 EXI pixels associated with an ACS-MIR profile (cf. Table 1). For all of them, we run the retrieval algorithm assuming the same typical uniform cloud profile (r_{eff} = 3 μm between 20 and 100 km) and profiles adjusted with inputs from ACS-MIR observations (altitude, size). In Section 3.1 we discuss the impact of the altitude of the clouds on the retrievals, and in Section 3.2 we also introduce a size gradient for the ice within the clouds.

Regarding the dust, we run the retrievals with uniform profiles of 1.5 μm particles uniformly distributed (with respect to the gas density) from the surface to two alternative altitudes for all of the observations: both 100 km as it is usually the case in such studies (e.g., Wolff et al., 2017, 2019, 2022) and, when using cloud altitudes from ACS-MIR profiles, the highest altitude without water ice detection below the clouds in the ACS-MIR profiles. Indeed, previous studies have shown that the dust in the atmosphere is essentially present below the higher water ice clouds (Smith et al., 2013; Luginin et al., 2020; Liuzzi et al., 2020; Stolzenbach et al., 2023). This is particularly important to consider for low-altitude clouds (in the polar regions) because the higher amount of dust particles at low altitudes will have a stronger impact on the τ_{cld} retrievals: more dust at the cloud altitude or above will "hide" the water ice by absorbing and scattering the light scattered by the water ice clouds, resulting in higher τ_{cld} in the retrievals.

For simplification purposes, in the following, even though some ACS-MIR profiles can exhibit multiple cloud layers (Stcherbinine et al.,

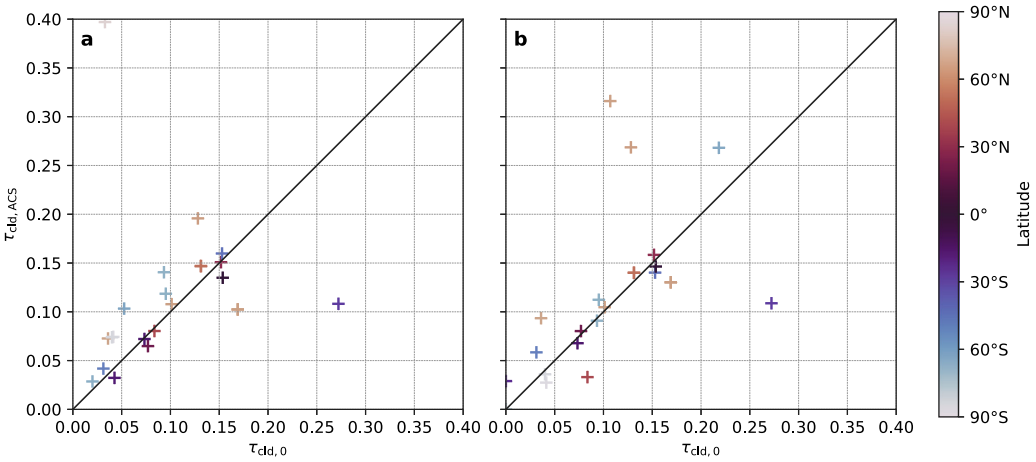

Fig. 3. EXI optical depth retrieved using clouds altitudes from ACS-MIR observations ($\tau_{cld,\ ACS}$) as a function of the optical depth retrieved using the typical cloud profile from 20 to 100 km ($\tau_{cld,\ 0}$). The color of the crosses shows the latitude of the associated observation, and the black line represents the $\tau_{cld,\ ACS} = \tau_{cld,\ 0}$ line. **a.** Dust particles are uniformly distributed from 0 to 100 km. **b.** Dust is only located below the clouds when using ACS-MIR altitudes. (For interpretation of the references to color in this figure legend, the reader is referred to the web version of this article.)

Table 1
List and coordinates of the 31 EXI and ACS-MIR observations used in this study. All observations have been acquired over MY 36.

EXI (XOS-1 – f320)	ACS-MIR	Longitude [°E]	Latitude [°N]	L_s [°]
20210724T220055	ORB016367_N1	72.2	−61.4	76.4
20210830T063840	ORB016809_N2	−133.7	−48.0	92.3
20211124T202544	ORB017868_N1	−146.9	−66.4	132.2
20211129T120020	ORB017925_N1	22.2	−65.7	134.4
20211201T132848	ORB017950_N1	28.4	−64.6	135.4
20211204T223121	ORB017991_N2	−9.9	40.8	137.1
20211206T172533	ORB018013_N2	70.2	30.4	138.0
20211208T130036	ORB018035_N1	132.9	−43.8	138.8
20220107T191342	ORB018403_N1	−103.4	−63.0	154.1
20220121T212521	ORB018576_N1	113.9	68.1	161.6
20220303T020711	ORB019068_N1	61.4	−86.6	183.7
20220307T100322	ORB019121_N1	−21.5	−83.9	186.2
20220323T024006	ORB019312_N1	−110.0	−68.6	195.3
20220407T071615	ORB019498_N1	−61.4	−22.9	204.3
20220424T012729	ORB019701_N2	32.8	−0.1	214.5
20220429T075125	ORB019766_N1	120.2	66.4	217.7
20220501T204754	ORB019797_N1	−52.0	66.9	219.3
20220515T082017	ORB019962_N1	−113.4	66.3	227.7
20220517T101316	ORB019987_N1	−110.8	65.9	229.0
20220531T055303	ORB020155_N2	6.2	−40.1	237.7
20220801T045738	ORB020913_N1	40.0	−12.2	276.9
20220805T165821	ORB020968_N1	−109.3	9.7	279.7
20220811T143523	ORB021039_N2	−167.2	20.9	283.3
20220812T064308	ORB021048_N1	98.3	37.2	283.8
20220818T212312	ORB021129_N1	−81.6	52.6	287.8
20220822T161908	ORB021174_N1	−113.0	−27.3	290.1
20220906T211836	ORB021361_N1	84.1	63.7	299.4
20220918T043109	ORB021499_N1	94.0	62.9	306.1
20220925T092024	ORB021587_N1	135.8	−14.5	310.3
20221213T193446	ORB022556_N2	−135.3	−15.8	353.6
20221223T220315	ORB022680_N1	93.5	83.5	358.8

2020, 2022), we will consider only one continuous cloud layer per profile for the retrievals, with the bottom and top altitudes corresponding respectively to the lowest and highest ice detections in the ACS-MIR atmospheric profile. However, if a profile exhibits multiple layers of water ice, we will consider that the maximum altitude for the dust is below the upper layer. Below this altitude, we will have a mix of dust and water ice particles, which is representative of what can be observed by the orbiters (e.g., Smith et al., 2013; Stcherbinine et al., 2020; Luginin et al., 2020; Stolzenbach et al., 2023).

3.1. Cloud altitudes

We define the following notations:

- $\tau_{cld,\ 0}$: optical depth retrieved assuming a typical constant profile with 3 μm water ice crystals uniformly distributed from 20 km to 100 km.
- $\tau_{cld,\ ACS}$: optical depth retrieved using clouds altitudes taken from ACS observations.
- $\Delta\tau_{cld} = \tau_{cld,\ 0} - \tau_{cld,\ ACS}$

Fig. 3 shows the EXI optical depth retrieved assuming 3 μm water ice particles at altitudes taken from ACS-MIR observations ($\tau_{cld,\ ACS}$) as a function of the optical depth retrieved using the typical constant profile from 20 to 100 km ($\tau_{cld,\ 0}$). We can see that globally, points associated with near-equatorial latitudes (darker points) are closer to the $y = x$ line and slightly below ($\tau_{cld,\ ACS} < \tau_{cld,\ 0}$) compared to the more polar observations (lighter points) that are more clearly above this line ($\tau_{cld,\ ACS} > \tau_{cld,\ 0}$). Adjusting the maximum altitude of the dust particles according to the altitude of the clouds for $\tau_{cld,\ ACS}$ (panel b) has two main effects on the distribution of the results: less scattering of around the $y = x$ line for retrievals associated with $\tau \sim 0.9 - 0.18$, but more difference between the two cases $\tau_{cld,\ ACS}$ and $\tau_{cld,\ 0}$ for smaller or larger values, especially for retrievals associated with observations performed with more polar latitudes.

Fig. 4 shows the difference ($\Delta\tau_{cld}$, panels a & b) and relative difference ($\Delta\tau_{cld}/\tau_{cld,\ 0}$, panels c & d) between EXI water ice clouds retrievals performed with the same typical cloud profile of 3 μm water ice particles uniformly distributed between 20 and 100 km, and with profiles whose altitudes are taken from contemporaneous ACS-MIR observations. Results are presented as a function of the minimum cloud altitude derived from the ACS-MIR observations (panels a & c) and the latitude of the observation (panels b & d). For the blue crosses, the bottom and top altitudes of the clouds are taken from ACS-MIR data but the upper altitude for the dust is still 100 km, and for the red crosses the dust is only present below the water ice clouds (with the minimum and maximum altitudes from ACS-MIR data). One can note that the total column-integrated dust optical depth remains the same in both cases, as it is taken from contemporaneous EMIRS observations.

We can see that the retrieved value of τ_{cld} depends on the altitude of the cloud provided in the model: for a given set of atmospheric and surface parameters, $\Delta\tau_{cld}$ decreases and increases along with the minimum altitude of the clouds, i.e., the value of τ_{cld} increases when the minimum altitude of the cloud decreases. Thus, if not accounting for the altitude of the clouds, the retrieval algorithm will underestimate the optical depth of the low-altitude clouds ($\Delta\tau_{cld} < 0$) and overestimate it for the high-altitude clouds ($\Delta\tau_{cld} > 0$), relatively to the bottom altitude assumed in the model, i.e., ~20 km. For clouds starting below ~10 km, τ_{cld} will be underestimated by 25% (up to 0.05 in absolute

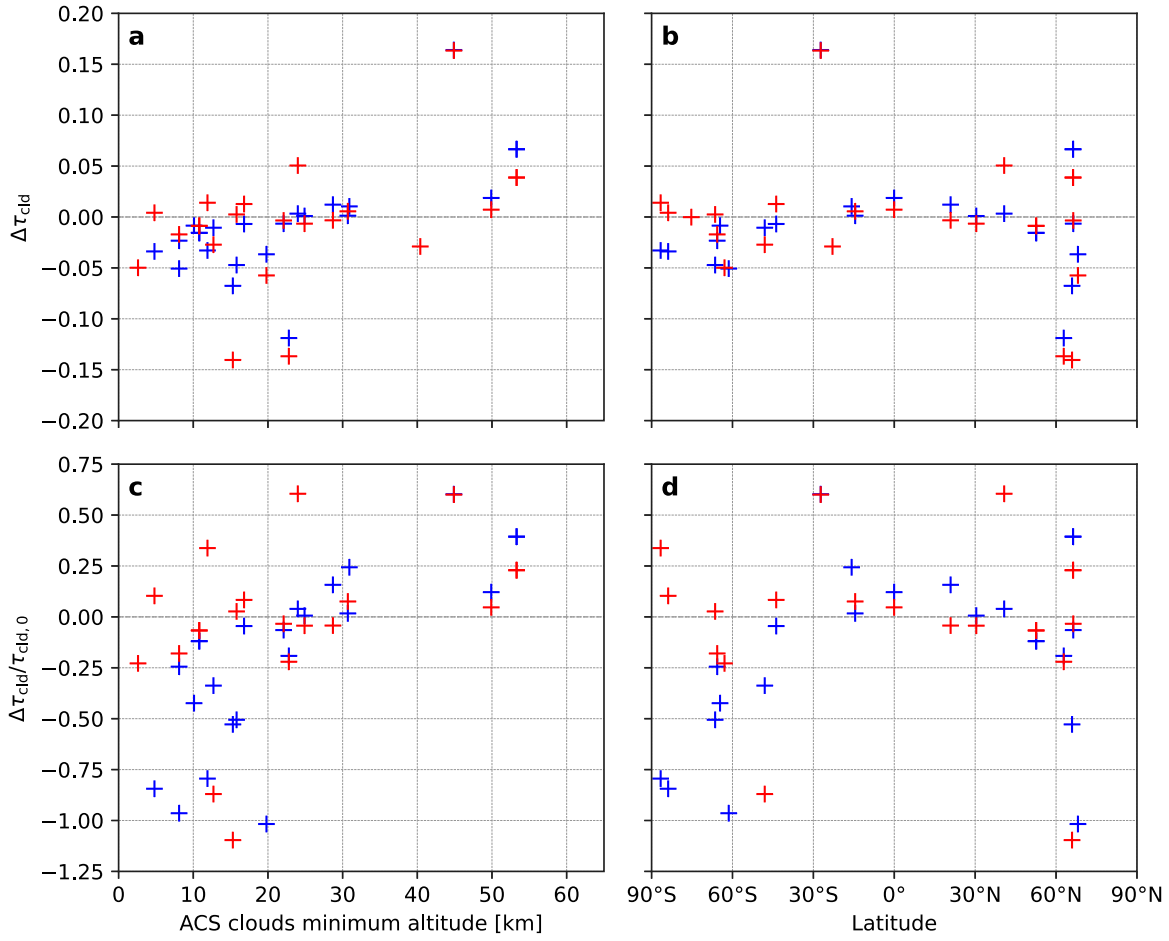

Fig. 4. a. & b. Difference between the τ_{cld} values retrieved from EXI observations assuming water ice clouds with particle size of 3 μm from 20 km to 100 km ($\tau_{cld,\,0}$) and the ones retrieved using top and bottom altitudes from ACS-MIR profiles ($\tau_{cld,\,ACS}$) and dust with particle size of 1.5 μm from 0 km to 100 km (blue), or dust only contained below the clouds (red). $\Delta\tau_{cld} = \tau_{cld,\,0} - \tau_{cld,\,ACS}$ **c. & d.** Same but normalized by the τ_{cld} values retrieved with clouds uniform between 20 km and 100 km (i.e., no ACS input). Results are displayed as a function of the clouds' minimum altitude from the ACS-MIR profiles (a & c) and the latitude of the observation (b & d). (For interpretation of the references to color in this figure legend, the reader is referred to the web version of this article.)

value), and similarly, for clouds with a bottom altitude between 40 and 60 km the τ_{cld} will be overestimated up to 50% (cf. Fig. 4 a & c). We also observe on Fig. 4 that, as expected, the retrievals are more affected by the dust profile for clouds with a minimum altitude below ~20 km (more difference between the blue and red points), and that the retrieved values of τ_{cld} decrease (i.e., $\Delta\tau_{cld}$ increase) when the dust is capped by the water ice clouds (red points are generally above the blue ones).

The altitude of the clouds varies significantly with the latitude (Forget et al., 1999; Heavens et al., 2011; Jaquin et al., 1986; Montmessin et al., 2006; Smith et al., 2013; Stcherbinine et al., 2022; Lolachi et al., 2022), which is visible in Fig. 1. Stcherbinine et al. (2022) reported that the typical altitude of the clouds is 20–40 km higher around the equator than in the polar regions, and that variations of the same order of magnitude also occur between summer and winter for both hemispheres. In our dataset, the minimum altitude of the clouds ranges from 3 km to 53 km. However, we do not have enough data here to discuss the impact of seasonal variations of the clouds.

As a consequence of the latitudinal variations of the cloud altitudes, the EXI nadir retrievals will tend to underestimate the τ_{cld} in the polar regions (up to ~25% if also decreasing the maximum altitude of the dust; ~50% otherwise) and slightly overestimate it around the equator (up to ~10% if also decreasing the maximum altitude of the dust; ~25% otherwise) if assuming the same uniform vertical profile between 20 and 100 km for all clouds (cf. Fig. 4 b & d). We can see that the red points have a smaller vertical scatter between the poles and the equator compared to the blue ones, which means that the amplitude of the variations in τ_{cld} when adjusting the altitude of the clouds is lowered if keeping the dust particles below the clouds. One should also note that the largest relative discrepancies between the retrievals observed in the polar regions are associated with absolute differences in the τ_{cld} values smaller than 0.05. The presence of optically thinner clouds in these regions contributes to enlarging the relative differences between the retrievals with and without taking into account the clouds and dust altitudes, but even the absolute variations $\Delta\tau_{cld}$ are still higher under polar latitudes as shown on Fig. 4b.

The sensitivity of τ_{cld} with the cloud altitudes is related to the presence of dust in the atmosphere. At low altitudes, the higher concentration of dust particles in the atmosphere will hide a larger fraction of the light scattered by the clouds. Thus, more water ice is required to reproduce the radiance observed from the orbit, which leads to thicker clouds in the retrievals. This explains the higher τ_{cld} values retrieved close to the poles when using the ACS altitudes for the clouds in the retrieval algorithm, where they are observed down to altitudes lower than 20 km. Also, as the density of dust particles decreases with the altitude (with respect to the CO_2 gas density) the distribution of the ice particles at high altitudes (typically above 50–60 km) will have a more limited impact on the τ_{cld} retrievals as these optically thinner layers will have a more minor contribution in the total column-integrated optical depth value. This explains why we observe such large variations in the retrieved τ_{cld} in the polar regions between computations with the dust altitude ranging up to 100 km, or only below the clouds. For instance, if

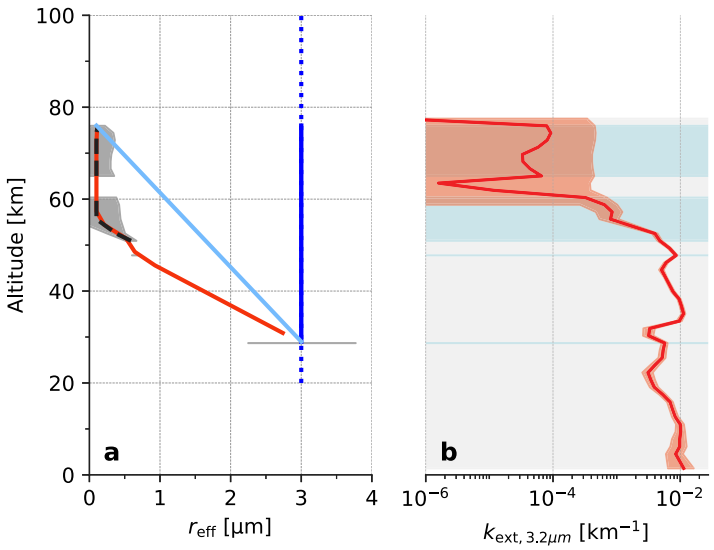

Fig. 5. **a.** Vertical r_{eff} profile (black dashed line) of a Martian cloud derived from ACS-MIR observation ORB021039_N2 (see Table 1) with the associated uncertainties (purple shaded areas) and sampled on the altitude grid used in the DISORT retrieval algorithm (red line), compared to the constant default profile using ACS-MIR altitudes (dark blue line) or the typical 20 to 100 km assumption (dark blue dotted line), and to the linear gradient profile using ACS-MIR altitudes (light blue line). **b.** Vertical profile of the atmospheric extinction coefficient (k_{ext}) at 3.2 µm (red line) derived from ACS-MIR observation ORB021039_2 with the associated uncertainties (red shaded area). The light blue areas represent the altitudes where water ice clouds have been identified. (For interpretation of the references to color in this figure legend, the reader is referred to the web version of this article.)

we look at the two clouds 87°S and 84°S, their ACS-MIR profiles report water ice between ~10 km and ~35 km, with the upper water ice layer starting from ~15 km. So at these altitudes where the particle density is higher (for both ice and dust), a few kilometers of dust mixed with water ice will have a strong impact on the retrievals by hiding the light reflected by the water ice particles.

3.2. Clouds particle sizes

We discussed in the previous section the impact of the altitude of the clouds on the EXI retrievals for a fixed value of r_{eff}. Here we use the altitude of the clouds as observed by ACS-MIR to focus on the impact of the size of the ice particles on the retrievals. More specifically, we focus on the vertical variations of the particle size within the cloud, rather than the choice of 3 µm as the default reference size for r_{eff}. Indeed, observational profiles of the Martian clouds by ACS-MIR have shown that they exhibit a decrease of the r_{eff} when the altitude increases, with sizes typically ranging from 2–3 µm at the bottom to 0.1 µm at the top (Stcherbinine et al., 2022, Figure 4).

Fig. 5 shows the comparison between a cloud profile obtained from ACS-MIR observations (ORB021039_N2) and the typical default for τ_{cld} retrievals in the literature, i.e., constant size of 3 µm from 20 to 100 km. We can see that if r_{eff} is similar at the bottom of the cloud (although ACS-MIR reported a cloud starting from 29 km only), it decreases quickly in the observations to reach 0.1 µm at 56 km and remain like so up to the top of the cloud at 79 km. In this section, we will discuss the impact of using different kinds of r_{eff} profiles for the clouds in DISORT on the retrieved τ_{cld}:

- Constant profile: r_{eff} remains constant regardless of the altitude, this is the assumption usually made for such nadir retrievals.
- Linear gradient profile: previous studies (e.g., Stcherbinine et al., 2020, 2022; Luginin et al., 2020; Liuzzi et al., 2020) have shown that the particle size within the clouds typically decreases down to ~0.1 µm when the altitude increases. Thus, we implemented an alternative r_{eff} profile where the water ice particle size decreases linearly when the altitude increases, ranging from a given value at the bottom altitude of the cloud to 0.1 µm at the top.

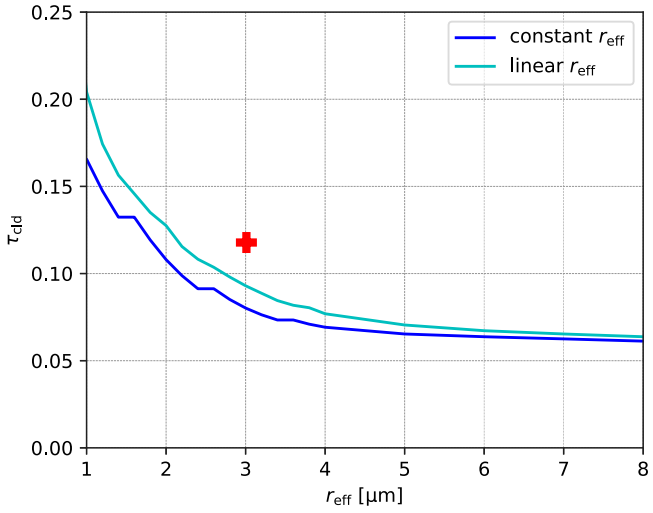

Fig. 6. Variation of the retrieved τ_{cld} value as a function of the water ice particle size within the cloud (EXI observation 20220811T143523) for a cloud with a constant particle size (blue line) or using a linear gradient from r_{eff} at the bottom of the cloud to 0.1 µm at the top (cyan line). The boundary altitudes of the cloud are taken from the corresponding ACS-MIR observation (ORB021039_N2), i.e., from 29 to 76 km, as well as the maximum altitude for the dust, set to 63 km. The red cross shows the result obtained using the actual ACS-MIR cloud profile shown in Fig. 5 (red line). (For interpretation of the references to color in this figure legend, the reader is referred to the web version of this article.)

- ACS-MIR profile: here we use the actual r_{eff} profile obtained from the correspondent ACS-MIR observation, resampled in the altitude grid used in the retrieval algorithm (cf. Fig. 5). As stated above and for simplification purposes, we consider the potential multiple layers that may be present in the ACS-MIR data as one single cloud layer, starting from the lowest altitude where water ice has been detected, and ending at the higher altitude with water ice.

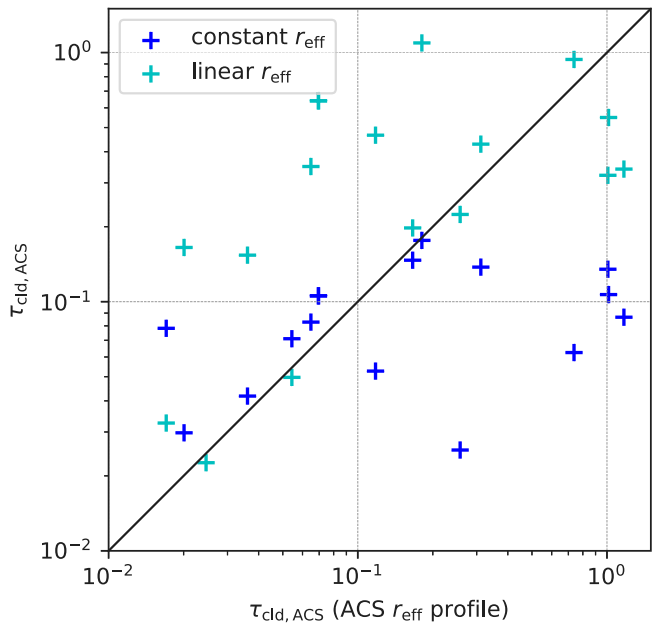

Fig. 7. EXI optical depth retrieved using clouds altitudes from ACS-MIR observations and either a constant r_{eff} profile of 3 μm (blue) or a linear gradient profile ranging from 3 μm at the bottom to 0.1 μm at the top (cyan) as a function of the optical depth retrieved using the actual corresponding ACS-MIR cloud profile. (For interpretation of the references to color in this figure legend, the reader is referred to the web version of this article.)

Fig. 6 shows the τ_{cld} values retrieved from the EXI observation 20220811T143523, using the cloud's altitude from ACS-MIR observation ORB021039_N2 (from 29 to 76 km), as a function of the water ice particle size assumed in the retrieval algorithm. These computations have been performed for both constant and linear gradient profiles, as well as using the actual ACS-MIR r_{eff} profile. We can see that the retrieved value for τ_{cld} depends on the assumed size of the water ice particles at the bottom of the cloud (either for the constant or the linear gradient case), especially for r_{eff} between 1 and 4 μm. It goes from $\tau_{cld} = 0.166$ for $r_{eff} = 1$ μm to $\tau_{cld} = 0.069$ for $r_{eff} = 4$ μm with the constant profile, and respectively from $\tau_{cld} = 0.204$ to $\tau_{cld} = 0.077$ with the linear gradient. For larger ice particles, from 4 to 8 μm, it became more stable: τ_{cld} goes from 0.069 to 0.061 for the constant profile, and from 0.077 to 0.064 for the linear gradient one.

We also observe that the difference between the constant and linear gradient profiles is more pronounced when only smaller ice particles are present in the cloud: the τ_{cld} values retrieved with the linear gradient profile are 10% to 20% larger than the results with the constant profile for $r_{eff} \leq 4$ μm, but the difference becomes smaller than 5% when r_{eff} at the bottom of the cloud is larger than 6 μm.

Smaller water ice particles in the clouds result in more reflective and less absorbing cloud layers in the atmosphere, which leads to thicker clouds retrieved in order to match the I/F measured values. Thus, introducing smaller particles in the upper part of the cloud with the linear gradient profile leads to an increase of the retrieved τ_{cld}. However, we can see that the increase of τ_{cld} due to the transition to a linear gradient profile is of lower magnitude compared to the decrease of r_{eff} at the bottom of the cloud. This can be explained by the fact that the density of particles in the atmosphere is higher at low altitudes, so the lower layers (also filled with more absorbent larger water ice particles) will dominate the column-integrated nadir optical depth of the clouds.

Fig. 6 also shows the τ_{cld} retrieved using the actual ACS-MIR profile as a matter of comparison (red cross). As we can see in Fig. 5, the ACS profile exhibits a decrease of r_{eff} from 3 μm at 29 km to 0.1 μm at 56 km, then the particle size remains at 0.1 μm up to the top of the cloud at 76 km. So, the proportion of very small water ice particles is higher in the ACS-MIR profile compared to the linear gradient one. Consequently, the value of τ_{cld} retrieved with this profile is larger than with the linear gradient profile for the same r_{eff} (3 μm): $\tau_{cld} = 0.118$ for the ACS-MIR profile versus $\tau_{cld} = 0.093$ for the linear gradient one (and $\tau_{cld} = 0.080$ for the constant profile). And so, even though it is not perfect, the use of a linear gradient instead of a constant profile for r_{eff} in the clouds retrievals improves the retrieved τ_{cld} by bringing it more than 40% closer to what can be obtained using the actual cloud profile.

The situation is more contrasted on a global view, as can be seen on Fig. 7, which shows the τ_{cld} values retrieved assuming either a constant r_{eff} profile (blue crosses) or a linear gradient (cyan crosses) between the boundary altitudes given by ACS-MIR observations, as a function of the τ_{cld} values retrieved using the actual ACS r_{eff} profiles. We can see that for the thinner clouds ($\tau_{cld} \lesssim 0.15$) the use of the constant profile can provide results closer to the τ_{cld} retrieved using the actual ACS-MIR profile compared to the linear gradient, but for thicker clouds it is better to consider a non-uniform r_{eff} profile. Actually, we observe in the figure that the uniform profile results in a smaller range of τ_{cld} (from 0.02 to 0.17) than the linear gradient one (from 0.02 to 1.05). For thicker clouds associated with $\tau_{cld} \gtrsim 0.15$, even though the τ_{cld} values retrieved using the ACS-MIR r_{eff} profiles increase (up to 1.2), the τ_{cld} values retrieved if assuming a constant profile do not exceed 0.18.

Thus, neither of the two tested profiles provides results perfectly in line with the ones obtained using the actual ACS-MIR r_{eff} profiles across the entire range of τ_{cld}. The linear gradient will result in lower precision for optically thin clouds, but the constant profile will fail to capture the thicker clouds. Further studies may try to discuss more advanced vertical profiles of r_{eff} such as exponential profiles, which may be closer to what has been observed by the orbiters (e.g., Stcherbinine et al., 2022).

4. Conclusion

In this paper, we use the combination of quasi-concomitant observations of the same region of the Martian atmosphere by the TGO/ACS-MIR and EMM/EXI instruments to study Martian water ice clouds, and discuss the impact of the refinement of the vertical structure of the clouds in radiative transfer models on optical depth retrievals performed from nadir imagery. The vertical distribution and properties of the aerosols and clouds in the atmosphere are two of the main hypotheses that have to be made in order to perform retrievals from nadir observations using radiative transfer algorithms. But this information can be retrieved from observations in different geometries, especially in Solar Occultation. Thus, we use cloud profiles (altitude and r_{eff}) obtained from ACS-MIR observations to perform optical depth (τ_{cld}) retrievals from EXI nadir images at 320 nm, and compare the results to the values obtained with a constant cloud profile typically used in this kind of study.

First, we show that not accounting for the variation of the clouds' altitude with the latitude that can be up to 40 km between the poles and the equator (Stcherbinine et al., 2022) leads to an underestimation of τ_{cld} up to 25% to 50% under polar latitudes, and an overestimation of about 10% to 25% at the equator if assuming a bottom altitude of 20 km for all the clouds (depending on the vertical distribution of the dust in the atmosphere).

Then, we show that the accounting for the variation of r_{eff} with the altitude in the clouds (with very small water ice particles at the top) also significantly affects the retrievals but to a lesser extent than altitude or the size of the ice particles at the bottom of the cloud. The retrieved values of τ_{cld} are dominated by the size of the larger water ice particles at low altitudes, but the impact of the very small ones at the top of the clouds is not negligible.

Thus, from the results presented in Section 3, we formulate two recommendations to improve the representation of Martian water ice clouds in radiative transfer models, and thereby the performed optical depth retrievals from nadir observations in future studies:

- Adjust the boundary altitudes of the clouds with latitude and season, from typical ranges that can be extracted from recent clouds' climatology, such as presented in Stcherbinine et al. (2022), and adjust the maximal altitude for the dust so it remains below the water ice clouds.
- Use of a non-constant r_{eff} profile for the clouds. For instance, a profile ranging from ~2–3 μm at the bottom to 0.1 μm at the top would provide a better representation of the vertical structure of the clouds and thus more accurate results for the thicker clouds, even if it is not perfect either. Future studies may even consider more evolved profiles for the vertical distribution of the water ice, with a non-linear decrease of r_{eff} that may be closer to what is observed by the orbiters (e.g., Stcherbinine et al., 2020, 2022; Liuzzi et al., 2020; Luginin et al., 2020; Stolzenbach et al., 2023).

This study is the first collaboration between the EMM and TGO/ACS science teams and paves the way for future synergies between these two active missions currently looking at the Martian atmosphere. And beyond that, it highlights the huge potential in developing more synergies between different spacecraft and instruments to study the Martian water ice clouds.

CRediT authorship contribution statement

Aurélien Stcherbinine: Writing – review & editing, Writing – original draft, Visualization, Validation, Software, Methodology, Investigation, Formal analysis, Data curation, Conceptualization. **Michael J. Wolff:** Writing – review & editing, Validation, Resources, Methodology, Conceptualization. **Christopher S. Edwards:** Writing – review & editing, Resources, Funding acquisition. **Oleg Korablev:** Writing – review & editing. **Anna Fedorova:** Writing – review & editing. **Alexander Trokhimovskiy:** Writing – review & editing.

Declaration of competing interest

The authors declare that they have no known competing financial interests or personal relationships that could have appeared to influence the work reported in this paper.

Data availability

Data from the Emirates Mars Mission (EMM) are freely and publicly available on the EMM Science Data Center (SDC, http://sdc.emiratesmarsmission.ae). This location is designated as the primary repository for all data products produced by the EMM team and is designated as long-term repository as required by the UAE Space Agency. The data available (http://sdc.emiratesmarsmission.ae/data) include ancillary spacecraft data, instrument telemetry, Level 1 (raw instrument data) to Level 3 (derived science products), quicklook products, and data users guides (https://sdc.emiratesmarsmission.ae/documentation) to assist in the analysis of the data. Following the creation of a free login, all EMM data are searchable via parameters such as product file name, solar longitude, acquisition time, sub-spacecraft latitude & longitude, instrument, data product level, etc. Data products can be browsed within the SDC via a standardized file system structure that follows the convention:
`/emm/data/<Instrument>/<DataLevel>/<Mode>/<Year>/<Month>` Data product filenames follow a standard convention:
`emm_<Instrument>_<DataLevel><StartTimeUTC>_<OrbitNumber>_<Mode>_<Description>_<Kernel-Level>_<Version>.<FileType>` EXI data and users guides are available at: https://sdc.emiratesmarsmission.ae/data/exi Raw ACS data are available on the ESA PSA at https://archives.esac.esa.int/psa/#!Table%20View/ACS=instrument.

Acknowledgments

This article is dedicated to the memory of Jessica Walsh. For the love of Mars and clouds.

This work was funded by the Emirates Mars Mission project under the Emirates Mars Infrared Spectrometer and the Emirates eXploration Images instruments via The United Arab Emirates Space Agency (UAESA) and the Mohammed bin Rashid Space Centre (MBRSC). A. S. also acknowledges funding by CNES.

ExoMars is a space mission of ESA and Roscosmos. The ACS experiment is led by IKI Space Research Institute in Moscow. The project acknowledges funding by Roscosmos and CNES. Science operations of ACS are funded by Roscosmos and ESA. Science support in IKI is funded by the Federal Agency of Science Organization (FANO).

References

Amiri, H.E.S., Brain, D., Sharaf, O., Withnell, P., McGrath, M., Alloghani, M., Al Awadhi, M., Al Dhafri, S., Al Hamadi, O., Al Matroushi, H., Al Shamsi, Z., Al Shehhi, O., Chaffin, M., Deighan, J., Edwards, C., Ferrington, N., Harter, B., Holsclaw, G., Kelly, M., Kubitschek, D., Landin, B., Lillis, R., Packard, M., Parker, J., Pilinski, E., Pramman, B., Reed, H., Ryan, S., Sanders, C., Smith, M., Tomso, C., Wrigley, R., Al Mazmi, H., Al Mheiri, N., Al Shamsi, M., Al Tunaiji, E., Badri, K., Christensen, P., England, S., Fillingim, M., Forget, F., Jain, S., Jakosky, B.M., Jones, A., Lootah, F., Luhmann, J.G., Osterloo, M., Wolff, M., Yousuf, M., 2022. The emirates mars mission. Space Sci. Rev. 218 (1), 4. http://dx.doi.org/10.1007/s11214-021-00868-x.

Atwood, S.A., Smith, M.D., Badri, K., Edwards, C.S., Christensen, P.R., Wolff, M.J., Forget, F., Anwar, S., Smith, N., El-Maarry, M.R., 2022. Diurnal variability in EMIRS daytime observations of water ice clouds during mars Aphelion-season. Geophys. Res. Lett. 49 (15), e2022GL099654. http://dx.doi.org/10.1029/2022GL099654.

Bell, III, J.F., Wolff, M.J., Malin, M.C., Calvin, W.M., Cantor, B.A., Caplinger, M.A., Clancy, R.T., Edgett, K.S., Edwards, L.J., Fahle, J., Ghaemi, F., Haberle, R.M., Hale, A., James, P.B., Lee, S.W., McConnochie, T., Noe Dobrea, E., Ravine, M.A., Schaeffer, D., Supulver, K.D., Thomas, P.C., 2009. Mars reconnaissance orbiter mars color imager (MARCI): instrument description, calibration, and performance. J. Geophys. Res.: Planets 114 (E8), http://dx.doi.org/10.1029/2008JE003315.

Clancy, R.T., Grossman, A.W., Wolff, M.J., James, P.B., Rudy, D.J., Billawala, Y.N., Sandor, B.J., Lee, S.W., Muhleman, D.O., 1996. Water vapor saturation at low altitudes around mars aphelion: a key to mars climate? Icarus 122 (1), 36–62. http://dx.doi.org/10.1006/icar.1996.0108.

Clancy, R.T., Wolff, M.J., Smith, M.D., Kleinböhl, A., Cantor, B.A., Murchie, S.L., Toigo, A.D., Seelos, K., Lefèvre, F., Montmessin, F., Daerden, F., Sandor, B.J., 2019. The distribution, composition, and particle properties of mars mesospheric aerosols: An analysis of CRISM visible/near-IR limb spectra with context from near-coincident MCS and MARCI observations. Icarus 328, 246–273. http://dx.doi.org/10.1016/j.icarus.2019.03.025.

Connour, K., Wolff, M., 2023. pyRT_DISORT: A pre-processing front-end to help make DISORT simulations easier in python. URL: https://github.com/kconnour/pyRT_DISORT.

Connour, K., Wolff, M.J., Schneider, N.M., Deighan, J., Lefèvre, F., Jain, S.K., 2022. Another one derives the dust: Ultraviolet dust aerosol properties retrieved from MAVEN/IUVS data. Icarus 387, 115177. http://dx.doi.org/10.1016/j.icarus.2022.115177.

Edwards, C.S., Christensen, P.R., Mehall, G.L., Anwar, S., Tunaiji, E.A., Badri, K., Bowles, H., Chase, S., Farkas, Z., Fisher, T., Janiczek, J., Kubik, I., Harris-Laurila, K., Holmes, A., Lazbin, I., Madril, E., McAdam, M., Miner, M., O'Donnell, W., Ortiz, C., Pelham, D., Patel, M., Powell, K., Shamordola, K., Tourville, T., Smith, M.D., Smith, N., Woodward, R., Weintraub, A., Reed, H., Pilinski, E.B., 2021. The emirates mars mission (EMM) emirates mars infrared spectrometer (EMIRS) instrument. Space Sci. Rev. 217 (7), 77. http://dx.doi.org/10.1007/s11214-021-00848-1.

Forget, F., Hourdin, F., Fournier, R., Hourdin, C., Talagrand, O., Collins, M., Lewis, S.R., Read, P.L., Huot, J.-P., 1999. Improved general circulation models of the Martian atmosphere from the surface to above 80 Km. J. Geophys. Res.: Planets 104 (E10), 24155–24175. http://dx.doi.org/10.1029/1999JE001025.

Goldman, A., Saunders, R., 1979. Analysis of atmospheric infrared spectra for altitude distribution of atmospheric trace constituents–I. Method of analysis. J. Quant. Spectrosc. Radiat. Transfer 21 (2), 155–161. http://dx.doi.org/10.1016/0022-4073(79)90027-X.

Haberle, R.M., Montmessin, F., Kahre, M.A., Hollingsworth, J.L., Schaeffer, J., Wolff, M.J., Wilson, R.J., 2011. Radiative effects of water ice clouds on the martian seasonal water cycle. In: Fourth International Workshop on the Mars Atmosphere: Modelling and Observations. Paris, France, pp. 223–226.

Hansen, J.E., Travis, L.D., 1974. Light scattering in planetary atmospheres. Space Sci. Rev. 16 (4), 527–610. http://dx.doi.org/10.1007/BF00168069.

Heavens, N.G., Richardson, M.I., Kleinböhl, A., Kass, D.M., McCleese, D.J., Abdou, W., Benson, J.L., Schofield, J.T., Shirley, J.H., Wolkenberg, P.M., 2011. The vertical distribution of dust in the martian atmosphere during northern spring and summer: Observations by the mars climate sounder and analysis of zonal average vertical dust profiles. J. Geophys. Res.: Planets 116 (E4), http://dx.doi.org/10.1029/2010JE003691.

Jaquin, F., Gierasch, P., Kahn, R., 1986. The vertical structure of limb hazes in the Martian atmosphere. Icarus 68 (3), 442–461. http://dx.doi.org/10.1016/0019-1035(86)90050-3.

Jones, A.R., Wolff, M., Alshamsi, M., Osterloo, M., Bay, P., Brennan, N., Bryant, K., Castleman, Z., Curtin, A., DeVito, E., Drake, V.A., Ebuen, D., Espejo, J., Farren, J., Fenton, B., Fisher, C., Fisher, M., Fortier, K., Gerwig, S., Heberlein, B., Jeppesen, C., Khoory, M.A., Knappmiller, S., Knavel, J., Koski, K., Looney, K., Lujan, P., Miller, M., Newcomb, G., Otzinger, G., Passe, H., Pilinski, E., Reed, H., Shuping, R., Sicken, P., Summers, D., Wade, S., Walton, L., Yaptengco, J.L., 2021. The emirates exploration imager (EXI) instrument on the emirates mars mission (EMM) hope mission. Space Sci. Rev. 217 (8), 81. http://dx.doi.org/10.1007/s11214-021-00852-5.

Korablev, O., Montmessin, F., Trokhimovskiy, A., Fedorova, A.A., Shakun, A.V., Grigoriev, A.V., Moshkin, B.E., Ignatiev, N.I., Forget, F., Lefèvre, F., Anufreychik, K., Dzuban, I., Ivanov, Y.S., Kalinnikov, Y.K., Kozlova, T.O., Kungurov, A., Makarov, V., Martynovich, F., Maslov, I., Merzlyakov, D., Moiseev, P.P., Nikolskiy, Y., Patrakeev, A., Patsaev, D., Santos-Skripko, A., Sazonov, O., Semena, N., Semenov, A., Shashkin, V., Sidorov, A., Stepanov, A.V., Stupin, I., Timonin, D., Titov, A.Y., Viktorov, A., Zharkov, A., Altieri, F., Arnold, G., Belyaev, D.A., Bertaux, J.L., Betsis, D.S., Duxbury, N., Encrenaz, T., Fouchet, T., Gérard, J.-C., Grassi, D., Guerlet, S., Hartogh, P., Kasaba, Y., Khatuntsev, I., Krasnopolsky, V.A., Kuzmin, R.O., Lellouch, E., Lopez-Valverde, M.A., Luginin, M., Määttänen, A., Marcq, E., Martin Torres, J., Medvedev, A.S., Millour, E., Olsen, K.S., Patel, M.R., Quantin-Nataf, C., Rodin, A.V., Shematovich, V.I., Thomas, I., Thomas, N., Vazquez, L., Vincendon, M., Wilquet, V., Wilson, C.F., Zasova, L.V., Zelenyi, L.M., Zorzano, M.P., 2018. The atmospheric chemistry suite (ACS) of three spectrometers for the ExoMars 2016 trace gas orbiter. Space Sci. Rev. 214 (1), 7. http://dx.doi.org/10.1007/s11214-017-0437-6.

Korablev, O., Vandaele, A.C., Montmessin, F., Fedorova, A.A., Trokhimovskiy, A., Forget, F., Lefèvre, F., Daerden, F., Thomas, I.R., Trompet, L., Erwin, J.T., Aoki, S., Robert, S., Neary, L., Viscardy, S., Grigoriev, A.V., Ignatiev, N.I., Shakun, A., Patrakeev, A., Belyaev, D.A., Bertaux, J.-L., Olsen, K.S., Baggio, L., Alday, J., Ivanov, Y.S., Ristic, B., Mason, J., Willame, Y., Depiesse, C., Hetey, L., Berkenbosch, S., Clairquin, R., Queirolo, C., Beeckman, B., Neefs, E., Patel, M.R., Bellucci, G., López-Moreno, J.-J., Wilson, C.F., Etiope, G., Zelenyi, L., Svedhem, H., Vago, J.L., The ACS and NOMAD Science Team, 2019. No detection of methane on Mars from early exomars trace gas orbiter observations. Nature 568 (7753), 517–520. http://dx.doi.org/10.1038/s41586-019-1096-4.

Lilensten, J., Dauvergne, J.L., Pellier, C., Delcroix, M., Beaudoin, E., Vincendon, M., Kraaikamp, E., Bertrand, G., Foster, C., Go, C., Kardasis, E., Pace, A., Peach, D., Wesley, A., Samara, E., Poedts, S., Colas, F., 2022. Observation from earth of an atypical cloud system in the upper Martian atmosphere. Astron. Astrophys. 661, A127. http://dx.doi.org/10.1051/0004-6361/202141735.

Liuzzi, G., Villanueva, G.L., Crismani, M.M.J., Smith, M.D., Mumma, M.J., Daerden, F., Aoki, S., Vandaele, A.C., Clancy, R.T., Erwin, J., Thomas, I., Ristic, B., Lopez-Moreno, J.-J., Bellucci, G., Patel, M.R., 2020. Strong variability of martian water ice clouds during dust storms revealed from ExoMars trace gas orbiter/NOMAD. J. Geophys. Res.: Planets 125 (4), e2019JE006250. http://dx.doi.org/10.1029/2019JE006250.

Lolachi, R., Irwin, P.G.J., Teanby, N.A., 2022. Vertical distribution of water vapour for Martian northern hemisphere summer in mars year 28 from mars climate sounder. Icarus 386, 115141. http://dx.doi.org/10.1016/j.icarus.2022.115141.

Luginin, M., Fedorova, A., Ignatiev, N., Trokhimovskiy, A., Shakun, A., Grigoriev, A., Patrakeev, A., Montmessin, F., Korablev, O., 2020. Properties of water ice and dust particles in the atmosphere of mars during the 2018 global dust storm as inferred from the atmospheric chemistry suite. J. Geophys. Res.: Planets 125 (11), e2020JE006419. http://dx.doi.org/10.1029/2020JE006419.

Määttänen, A., Listowski, C., Montmessin, F., Maltagliati, L., Reberac, A., Joly, L., Bertaux, J.-L., 2013. A complete climatology of the aerosol vertical distribution on Mars from MEx/SPICAM UV solar occultations. Icarus 223 (2), 892–941. http://dx.doi.org/10.1016/j.icarus.2012.12.001.

Madeleine, J.-B., Forget, F., Millour, E., Navarro, T., Spiga, A., 2012. The influence of radiatively active water ice clouds on the Martian climate. Geophys. Res. Lett. 39 (23), http://dx.doi.org/10.1029/2012GL053564.

Malin, M.C., Bell, III, J.F., Calvin, W., Clancy, R.T., Haberle, R.M., James, P.B., Lee, S.W., Thomas, P.C., Caplinger, M.A., 2001. Mars color imager (MARCI) on the mars climate orbiter. J. Geophys. Res.: Planets 106 (E8), 17651–17672. http://dx.doi.org/10.1029/1999JE001145.

Mateshvili, N., Fussen, D., Vanhellemont, F., Bingen, C., Dodion, J., Montmessin, F., Perrier, S., Dimarellis, E., Bertaux, J.-L., 2007. Martian ice cloud distribution obtained from SPICAM nadir UV measurements. J. Geophys. Res.: Planets 112 (E7), http://dx.doi.org/10.1029/2006JE002827.

Montmessin, F., Forget, F., Rannou, P., Cabane, M., Haberle, R.M., 2004. Origin and role of water ice clouds in the Martian water cycle as inferred from a general circulation model. J. Geophys. Res.: Planets 109 (E10), http://dx.doi.org/10.1029/2004JE002284.

Montmessin, F., Korablev, O., Lefèvre, F., Bertaux, J.L., Fedorova, A., Trokhimovskiy, A., Chaufray, J.Y., Lacombe, G., Reberac, A., Maltagliati, L., Willame, Y., Guslyakova, S., Gérard, J.C., Stiepen, A., Fussen, D., Mateshvili, N., Määttänen, A., Forget, F., Witasse, O., Leblanc, F., Vandaele, A.C., Marcq, E., Sandel, B., Gondet, B., Schneider, N., Chaffin, M., Chapron, N., 2017a. SPICAM on mars express: A 10 year in-depth survey of the Martian atmosphere. Icarus 297, 195–216. http://dx.doi.org/10.1016/j.icarus.2017.06.022.

Montmessin, F., Quémerais, E., Bertaux, J.L., Korablev, O., Rannou, P., Lebonnois, S., 2006. Stellar occultations at UV wavelengths by the SPICAM instrument: Retrieval and analysis of martian haze profiles. J. Geophys. Res. 111 (E9), http://dx.doi.org/10.1029/2005JE002662.

Montmessin, F., Smith, M.D., Langevin, Y., Mellon, M.T., Fedorova, A., 2017b. The water cycle. In: Forget, F.c., Smith, M.D., Clancy, R.T., Zurek, R.W., Haberle, R.M. (Eds.), The Atmosphere and Climate of Mars. In: Cambridge Planetary Science, Cambridge University Press, Cambridge, pp. 338–373. http://dx.doi.org/10.1017/9781139060172.011.

Navarro, T., Madeleine, J.-B., Forget, F., Spiga, A., Millour, E., Montmessin, F., Määttänen, A., 2014. Global climate modeling of the Martian water cycle with improved microphysics and radiatively active water ice clouds. J. Geophys. Res.: Planets 119 (7), 1479–1495. http://dx.doi.org/10.1002/2013JE004550.

Rannou, P., Perrier, S., Bertaux, J.-L., Montmessin, F., Korablev, O., Rébérac, A., 2006. Dust and cloud detection at the Mars limb with UV scattered sunlight with SPICAM. J. Geophys. Res.: Planets 111 (E9), http://dx.doi.org/10.1029/2006JE002693.

Saito, M., Yang, P., Ding, J., Liu, X., 2021. A comprehensive database of the optical properties of irregular aerosol particles for radiative transfer simulations. J. Atmos. Sci. 78 (7), 2089–2111. http://dx.doi.org/10.1175/JAS-D-20-0338.1.

Smith, M.D., Badri, K., Atwood, S.A., Edwards, C.S., Christensen, P.R., Wolff, M.J., Bertrand, T., Forget, F., Al Tunaiji, E., Wolfe, C., Smith, N., Anwar, S., 2022. EMIRS observations of the aphelion-season mars atmosphere. Geophys. Res. Lett. 49 (15), e2022GL099636. http://dx.doi.org/10.1029/2022GL099636.

Smith, M.D., Bandfield, J.L., Christensen, P.R., Richardson, M.I., 2003. Thermal emission imaging system (THEMIS) infrared observations of atmospheric dust and water ice cloud optical depth. J. Geophys. Res.: Planets 108 (E11), http://dx.doi.org/10.1029/2003JE002115.

Smith, M.D., Pearl, J.C., Conrath, B.J., Christensen, P.R., 2001. One Martian year of atmospheric observations by the thermal emission spectrometer. Geophys. Res. Lett. 28 (22), 4263–4266. http://dx.doi.org/10.1029/2001GL013608.

Smith, M.D., Wolff, M.J., Clancy, R.T., Kleinböhl, A., Murchie, S.L., 2013. Vertical distribution of dust and water ice aerosols from CRISM limb-geometry observations: CRISM LIMB AEROSOLS. J. Geophys. Res.: Planets 118 (2), 321–334. http://dx.doi.org/10.1002/jgre.20047.

Stamnes, K., Tsay, S.C., Jayaweera, K., Wiscombe, W., Stamnes, S., Jin, Z., Lin, Z., 2017. DISORT: discrete ordinate radiative transfer. Astrophys. Source Code Libr. ascl:1708.006.

Stamnes, K., Tsay, S.-C., Wiscombe, W., Jayaweera, K., 1988. Numerically stable algorithm for discrete-ordinate-method radiative transfer in multiple scattering and emitting layered media. Appl. Opt. 27 (12), 2502–2509. http://dx.doi.org/10.1364/AO.27.002502.

Stcherbinine, A., 2022. A two martian years survey of water ice clouds on mars with ACS onboard TGO. http://dx.doi.org/10.17632/hff8kc6fsy.1, v1.

Stcherbinine, A., Montmessin, F., Vincendon, M., Wolff, M.J., Vals, M., Korablev, O., Fedorova, A., Trokhimovskiy, A., Lacombe, G., Baggio, L., 2022. A two martian years survey of water ice clouds on mars with ACS onboard TGO. J. Geophys. Res.: Planets 127 (12), e2022JE007502. http://dx.doi.org/10.1029/2022JE007502.

Stcherbinine, A., Vincendon, M., Montmessin, F., Wolff, M.J., Korablev, O., Fedorova, A., Trokhimovskiy, A., Patrakeev, A., Lacombe, G., Baggio, L., Shakun, A., 2020. Martian water ice clouds during the 2018 global dust storm as observed by the ACS-mir channel onboard the trace gas orbiter. J. Geophys. Res.: Planets 125 (3), e2019JE006300. http://dx.doi.org/10.1029/2019JE006300.

Stevens, M.H., Siskind, D.E., Evans, J.S., Jain, S.K., Schneider, N.M., Deighan, J., Stewart, A.I.F., Crismani, M., Stiepen, A., Chaffin, M.S., McClintock, W.E., Holsclaw, G.M., Lefèvre, F., Lo, D.Y., Clarke, J.T., Montmessin, F., Jakosky, B.M., 2017. Martian mesospheric cloud observations by IUVS on MAVEN: thermal tides coupled to the upper atmosphere: IUVS martian mesospheric clouds. Geophys. Res. Lett. 44 (10), 4709–4715. http://dx.doi.org/10.1002/2017GL072717.

Stolzenbach, A., López Valverde, M.-A., Brines, A., Modak, A., Funke, B., González-Galindo, F., Thomas, I., Liuzzi, G., Villanueva, G., Luginin, M., Aoki, S., Grabowski, U., Lopez Moreno, J.J., Rodriguez-Gomez, J., Wolff, M., Ristic, B., Daerden, F., Bellucci, G., Patel, M., Vandaele, A.-C., 2023. Martian atmospheric aerosols composition and distribution retrievals during the first martian year of NOMAD/TGO solar occultation measurements: 2. Extended results, end of MY 34 and first half of MY 35. J. Geophys. Res.: Planets 128 (11), e2023JE007835. http://dx.doi.org/10.1029/2023JE007835.

Szantai, A., Audouard, J., Forget, F., Olsen, K.S., Gondet, B., Millour, E., Madeleine, J.-B., Pottier, A., Langevin, Y., Bibring, J.-P., 2021. Martian cloud climatology and life cycle extracted from mars express OMEGA spectral images. Icarus 353, 114101. http://dx.doi.org/10.1016/j.icarus.2020.114101.

Trokhimovskiy, A., Korablev, O., Ivanov, Y.S., Siniyavsky, I.I., Fedorova, A., Stepanov, A.V., Titov, A.Y., Patrakeev, A., Moiseev, P.P., Kozlova, T.O., Montmessin, F., 2015. Middle-infrared echelle cross-dispersion spectrometer ACS-MIR for the ExoMars Trace Gas Orbiter. In: Strojnik Scholl, M., Páez, G. (Eds.), SPIE Optical Engineering + Applications. San Diego, California, United States, 960808. http://dx.doi.org/10.1117/12.2190359.

Vandaele, A.C., Korablev, O., Daerden, F., Aoki, S., Thomas, I.R., Altieri, F., López-Valverde, M., Villanueva, G., Liuzzi, G., Smith, M.D., Erwin, J.T., Trompet, L., Fedorova, A.A., Montmessin, F., Trokhimovskiy, A., Belyaev, D.A., Ignatiev, N.I., Luginin, M., Olsen, K.S., Baggio, L., Alday, J., Bertaux, J.-L., Betsis, D., Bolsée, D., Clancy, R.T., Cloutis, E., Depiesse, C., Funke, B., Garcia-Comas, M., Gérard, J.-C., Giuranna, M., Gonzalez-Galindo, F., Grigoriev, A.V., Ivanov, Y.S., Kaminski, J., Karatekin, O., Lefèvre, F., Lewis, S., López-Puertas, M., Mahieux, A., Maslov, I., Mason, J., Mumma, M.J., Neary, L., Neefs, E., Patrakeev, A., Patsaev, D., Ristic, B., Robert, S., Schmidt, F., Shakun, A., Teanby, N.A., Viscardy, S., Willame, Y., Whiteway, J., Wilquet, V., Wolff, M.J., Bellucci, G., Patel, M.R., López-Moreno, J.-J., Forget, F., Wilson, C.F., Svedhem, H., Vago, J.L., Rodionov, D., NOMAD Science Team, ACS Science Team, 2019. Martian dust storm impact on atmospheric H2O and D/H observed by ExoMars trace gas orbiter. Nature 568 (7753), 521–525. http://dx.doi.org/10.1038/s41586-019-1097-3.

Vincendon, M., Gondet, B., Pilorget, C., Langevin, Y., 2011a. Spatial, seasonal and vertical distribution of water ice cloud particle size infered from OMEGA limb data. pp. 207–208.

Vincendon, M., Pilorget, C., Gondet, B., Murchie, S., Bibring, J.-P., 2011b. New near-IR observations of mesospheric CO_2 and H_2 O clouds on Mars. J. Geophys. Res. 116, http://dx.doi.org/10.1029/2011JE003827.

Willame, Y., Vandaele, A.C., Depiesse, C., Lefèvre, F., Letocart, V., Gillotay, D., Montmessin, F., 2017. Retrieving cloud, dust and ozone abundances in the Martian atmosphere using SPICAM/UV nadir spectra. Planet. Space Sci. 142, 9–25. http://dx.doi.org/10.1016/j.pss.2017.04.011.

Wilson, R.J., Lewis, S.R., Montabone, L., Smith, M.D., 2008. Influence of water ice clouds on Martian tropical atmospheric temperatures. Geophys. Res. Lett. 35 (7), http://dx.doi.org/10.1029/2007GL032405.

Wilson, R.J., Neumann, G.A., Smith, M.D., 2007. Diurnal variation and radiative influence of Martian water ice clouds. Geophys. Res. Lett. 34 (2), http://dx.doi.org/10.1029/2006GL027976.

Wolff, M.J., Clancy, R.T., 2003. Constraints on the size of Martian aerosols from thermal emission spectrometer observations. J. Geophys. Res.: Planets 108 (E9), http://dx.doi.org/10.1029/2003JE002057.

Wolff, M.J., Clancy, R.T., Kahre, M.A., Haberle, R.M., Forget, F., Cantor, B.A., Malin, M.C., 2019. Mapping water ice clouds on Mars with MRO/MARCI. Icarus 332, 24–49. http://dx.doi.org/10.1016/j.icarus.2019.05.041.

Wolff, M.J., Fernando, A., Smith, M.D., Forget, F., Millour, E., Atwood, S.A., Jones, A.R., Osterloo, M.M., Shuping, R., Al Shamsi, M., Jeppesen, C., Fisher, C., 2022. Diurnal variations in the aphelion cloud belt as observed by the emirates exploration imager (EXI). Geophys. Res. Lett. 49 (18), e2022GL100477. http://dx.doi.org/10.1029/2022GL100477.

Wolff, M.J., Lopéz-Valverde, M., Madeleine, J.-B., Wilson, R.J., Smith, M.D., Fouchet, T., Delory, G.T., 2017. Radiative process: techniques and applications. In: Forget, F.c., Smith, M.D., Clancy, R.T., Zurek, R.W., Haberle, R.M. (Eds.), The Atmosphere and Climate of Mars. In: Cambridge Planetary Science, Cambridge University Press, Cambridge, pp. 106–171. http://dx.doi.org/10.1017/9781139060172.006.

Wolff, M.J., Todd Clancy, R., Goguen, J.D., Malin, M.C., Cantor, B.A., 2010. Ultraviolet dust aerosol properties as observed by MARCI. Icarus 208 (1), 143–155. http://dx.doi.org/10.1016/j.icarus.2010.01.010.